ADVANCED OPTICAL MATERIALS
www.advopticalmat.de

Deep Convolutional Neural Networks to Predict Mutual Coupling Effects in Metasurfaces

Sensong An, Bowen Zheng, Mikhail Y. Shalaginov, Hong Tang, Hang Li, Li Zhou, Yunxi Dong, Mohammad Haerinia, Anuradha Murthy Agarwal, Clara Rivero-Baleine, Myungkoo Kang, Kathleen A. Richardson, Tian Gu, Juejun Hu, Clayton Fowler, and Hualiang Zhang**

Metasurfaces have provided a novel and promising platform for realizing compact and high-performance optical devices. The conventional metasurface design approach assumes periodic boundary conditions for each element, which is inaccurate in most cases since near-field coupling effects between elements will change when the element is surrounded by nonidentical structures. In this paper, a deep learning approach is proposed to predict the actual electromagnetic (EM) responses of each target meta-atom placed in a large array with near-field coupling effects taken into account. The predicting neural network takes the physical specifications of the target meta-atom and its neighbors as input, and calculates its actual phase and amplitude in milliseconds. This approach can be used to optimize metasurfaces' efficiencies when combined with optimization algorithms. To demonstrate the efficacy of this methodology, large improvements in efficiency for a beam deflector and a metalens over the conventional design approach are obtained. Moreover, it is shown that the correlations between a metasurface's performance and its design errors caused by mutual coupling are not bound to certain specifications (materials, shapes, etc.). As such, it is envisioned that this approach can be readily applied to explore the mutual coupling effects and improve the performance of various metasurface designs.

1. Introduction

Metamaterials, along with their 2D versions, metasurfaces, have attracted wide attentions in recent years due to their unique low profile and lightweight properties as compared to their conventional bulk optics counterparts. Meta-atoms, the building blocks of metasurfaces, constructed with either all-dielectric[1–3] or plasmonic[4–6] nanoresonators, are capable of achieving engineered phase and amplitude control at the element level and thus enable accurate wave front control with subwavelength resolution. The most widely adopted metasurface design approach includes two steps: 1) calculate the amplitude and phase masks necessary for desired functionalities, fitted to square or hexagonal grids, and 2) find meta-atoms with performance closest to the target of each grid for the final design. Accurate and efficient meta-atom on-demand design approaches remain the main challenge with metasurface designs.

To design meta-atoms with maximum efficiency and accurate phase gradients, a common method is to consider structures with simple geometric shapes (such as circles,[7,8] rectangles,[9,10] H-shapes,[11,12] and plasmonic thin layers[13,14]) and perform a parameter sweep over all dimensions to assemble a library covering the full design space. Then best-fit meta-atoms are selected from the library to approximate the ideal amplitude/phase map. Beyond this brute-force approach, previous literatures have also reported metasurface designs that based on solid physical considerations, such as waveguiding analysis,[15,16] Huygens surface,[11,17] surface integral equations,[18–20] and Pancharatnam–Berry (PB) phase.[4,21] In

S. An, B. Zheng, H. Tang, H. Li, L. Zhou, Y. Dong, M. Haerinia, C. Fowler, H. Zhang
Department of Electrical & Computer Engineering
University of Massachusetts Lowell
Lowell, MA 01854, USA
E-mail: clayton_fowler@uml.edu; hualiang_zhang@uml.edu
S. An, M. Y. Shalaginov, A. M. Agarwal, J. Hu
Department of Materials Science & Engineering
Massachusetts Institute of Technology
Cambridge, MA 02139, USA
The ORCID identification number(s) for the author(s) of this article can be found under https://doi.org/10.1002/adom.202102113.
A. M. Agarwal, T. Gu, J. Hu
Materials Research Laboratory
Massachusetts Institute of Technology
Cambridge, MA 02139, USA
C. Rivero-Baleine
Lockheed Martin Corporation
Orlando, FL 32819, USA
M. Kang, K. A. Richardson
College of Optics and Photonics
CREOL
University of Central Florida
Orlando, FL 32816, USA

DOI: 10.1002/adom.202102113

addition to these methods, recently numerous optimization algorithms,[22–26] deep neural networks (DNN),[27–33] and DNN-optimization adjoint methods[34–36] have also been proposed recently for the fast inverse design of meta-atoms with complex shapes or multiple objectives.[37] In these meta-atom design approaches mentioned above, unit cell boundary conditions were adopted during full wave simulations, which assumes that each meta-atom structure under consideration is part of an infinite 2D array of identical structures. Thus, the amplitude and phase response calculations of the meta-atoms are based on the assumption that near-field coupling perturbations originate from identical neighbors. However, in real metasurface designs, each meta-atom is usually surrounded by nonidentical meta-atoms, for which near-field coupling effects will differ from those used to calculate the original response. As a result, the phase and amplitude of each meta-atom will be perturbed from their predicted values; thus, this method is accurate only when the mutual coupling effects between each meta-atom and its neighbors are vanishingly small, which is generally not the case. We examine and illustrate near-field mutual coupling effects between several types of meta-atoms, including circles,[7,8] rectangles,[9] and C-shaped thin layers[6] in Figure S1 (Supporting Information).

In previous work, instances have been reported where the mutual coupling effect (either radiative coupling[38] or dipole coupling) plays such an important role in a metasurfaces' overall performance that measures must be taken to minimize its effect. In ref. [8], a periodic arrangement of 2×2 meta-atoms was adopted in order to decrease the coupling effects in a metasurface hologram, while in ref. [39], the metasurface hologram was divided into several 17.35×17.35 μm^2 subarrays each constructed with identical meta-atoms. In ref. [40], the height and diameters of the cylindrical meta-atoms that formed the metasurface beam deflector were slightly adjusted to achieve higher efficiency. In ref. [41], a genetic algorithm (GA) was employed to find the meta-atoms' optimal dimensions and positions with strong coupling between neighbors taken into consideration. In some other works, the mutual coupling effects between adjacent meta-atoms were not only investigated, but also utilized to enhance the metasurfaces' performance. In ref. [42], a strongly coupled resonator design was proposed and demonstrated in the terahertz and optical regimes, in which the coupling between neighboring resonators was tuned to enhance the effective refractive index. In ref. [43], the near-field effects in high-index Mie-resonant nanoparticles were studied, and the distances between neighboring meta-atoms were tuned to realize continuous relative phase changes. In ref. [44], a deep neural network was trained to predict the electric field of each 50×50 μm^2 square area in a full-scale metasurface, which accounted for the interscatterer coupling effect. In ref. [45], a numerical method (so-called local phase method (LPM)) was proposed to obtain the phase of each meta-atom within the metasurfaces while considering the mutual coupling effects. This approach quantifies the phase error of each element inside the metasurfaces, which enables the optimization of metasurfaces on an element level while accounting for near-field coupling effects. While it provides a way to measure the meta-atoms' accurate phase responses, the target meta-atom and all its neighbors need to be simulated as a whole in order to derive the performance of a single meta-atom, which is computationally intensive and time consuming.

In this paper, we propose a DNN approach to efficiently predict the meta-atoms' phase and amplitude responses while accounting for the influence of its neighbors. When fully trained, the DNN is able to predict the perturbed EM response of a meta-atom given the dimensions of itself and its neighbors. Importantly, the accurate forward predictions can be achieved in milliseconds, which enables the fast optimization of various metasurface devices, including beam deflectors, lenses, and holograms that are composed of densely arranged meta-atoms prone to amplitude drop or phase error caused by mutual coupling. To demonstrate the efficacy of this DNN approach, we employed the fully trained DNN to optimize several beam deflectors and focusing lenses, demonstrating significant performance improvement compared to the conventional approaches.

2. Data Collection

Without loss of generality, we started our analysis with the transmissive all-dielectric metasurface design presented,[9] which is comprised of rectangular-shaped high-index (n = 3.67) polysilicon nanoblocks sitting on a low-index (n = 1.45) fused silica substrate (**Figure 1**a). The wavelength of interest is 1.55 μm, with the lattice constant of 800 nm and nanoblock height of 270 nm. By carefully selecting the length and width of each nanoblock, this meta-atom design can cover full 2π phase while maintaining high transmission, an essential condition for most optical applications. First, the actual phase and amplitude response of randomly-generated meta-atoms placed among different random neighbors (hereinafter referred to as "local responses") were calculated to assemble the training dataset. Simulation of each group of data starts by modeling the entire structure (Figure 1b), which includes the target meta-atom and its neighbors, using the commercial software CST (Figure 1c). The equivalent sources (J_s,M_s) of the target meta-atom were then obtained (by the Field Source Monitor in CST) and imported into a new model, with periodic boundary conditions applied to both x and y directions and open boundary condition applied to $\pm z$ directions (Figure 1d). A probe was placed on the broad side of the equivalent source, to measure the local amplitude and phase responses of the target meta-atom. The probe was placed more than 5 wavelength away from the source to ensure it's in the far field. For simplicity, the problem was limited to 1D, meaning only coupling effects along the x-axis (as shown in Figure 1) were considered, and periodic boundary conditions were set along the y-axis.

Considering that mutual coupling effects decrease with distance, it is necessary to determine the number of neighboring meta-atoms that needs to be considered in each simulation. To strike a balance between simulation accuracy and optimization difficulty (as well as data collection costs), 4 neighbors on each side of the target meta-atom were considered during the data collection process (Detailed discussions can be found in the Supporting Information Section I). The final dataset was composed of the physical dimensions and local responses of over 100 000 randomly-generated meta-atoms that were each

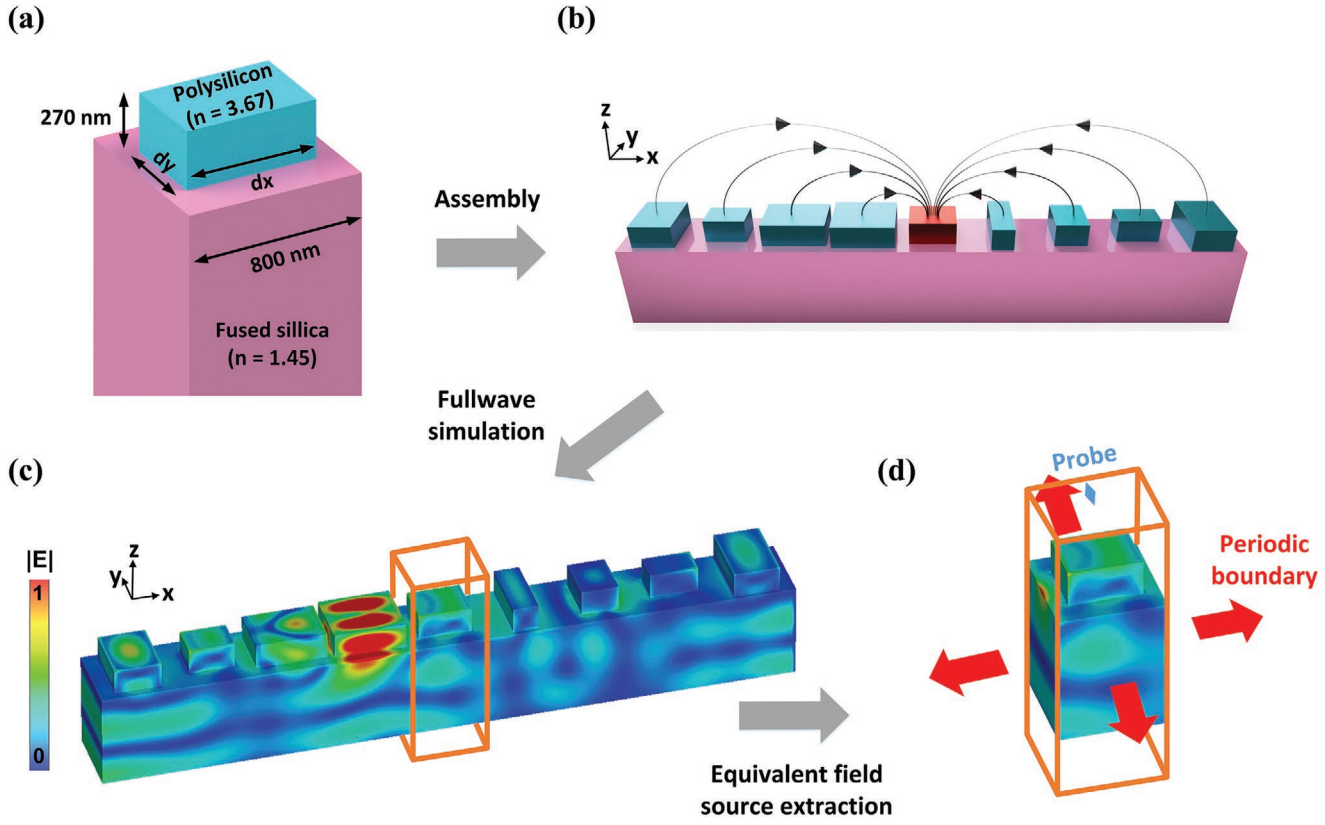

Figure 1. Data collection process. a) Schematic of a meta-atom represented as a silicon nanoblock on top of fused silica substrate. b) Randomly generated target meta-atoms (red) surrounded by random neighbors (blue) on each side. c) Simulated E-field of the whole structure. d) The extracted equivalent field source of target meta-atom. A probe was placed in the far field to measure the EM responses.

surrounded by 4 randomly-generated meta-atoms on each side. The lengths (dx) and widths (dy) of all nanoblocks were within the range of [0.25, 0.75 μm] with a minimum step of 6.25 nm. The local responses of the center meta-atom remains unchanged when the whole structure rotates by 180°, so the number of training data can be doubled by including input patterns that were flipped in the left-right direction.

3. Network Architecture

In order to realize fast prediction of meta-atoms' local responses under various boundary conditions, a predicting neural network (PNN) was constructed based on a convolutional neural network (CNN) architecture. The PNN takes the dimensions of the target meta-atom and dimensions of its neighbors as input, and quickly predicts local responses of target meta-atoms. As shown in **Figure 2**, 2D cross sections of the target meta-device were extracted and pixelated into an 1152 × 128 image. The image is binarized such that 1's represent dielectric regions and 0's represent voids. This figure was then processed through 6 consecutive convolutional layers, during which hidden features such as relationships between the nanoblock's dimensions and its local responses as well as the impact of its neighbors were extracted and calculated. After flattening the output of the CNNs into a 1D vector and passing through 3 fully connected layers, the prediction results for the complex transmission coefficients of the target meta-atom were generated. Throughout the network, a ReLU activation function was applied to each layer except for the last one, for which there was no activation function.

The over 200 000 groups of the collected training data were randomly split into a training set and a test set, containing 70% and 30% of the total training data, respectively. The test set was used to evaluate the trained network's performance on data that was not used during training. During training, the PNN-predicted local responses were compared with the labels (accurate local responses) to calculate the mean square error (MSE), defined as

$$\mathrm{MSE} = \frac{1}{N}\sum_{i=1}^{N}\sqrt{\left(y_i - \hat{y}_i\right)^2} \tag{1}$$

which was minimized by inversely tuning the parameters in the hidden neural layers. When the training was completed, the MSE was 9×10^{-6} for the training set and 7×10^{-5} for the test set, respectively (**Figure 3**a), which corresponds to an average prediction standard deviation of 0.005 for amplitude and 3.15° for phase at the target wavelength for each target meta-atom. We demonstrate the accuracy of the well-trained PNN with several samples that were randomly selected from the test set. As shown in Figure 3b, six target meta-atoms (marked with red) surrounded by 4 different meta-atoms on each side (marked in yellow) were set as input of the fully-trained PNN. The PNN

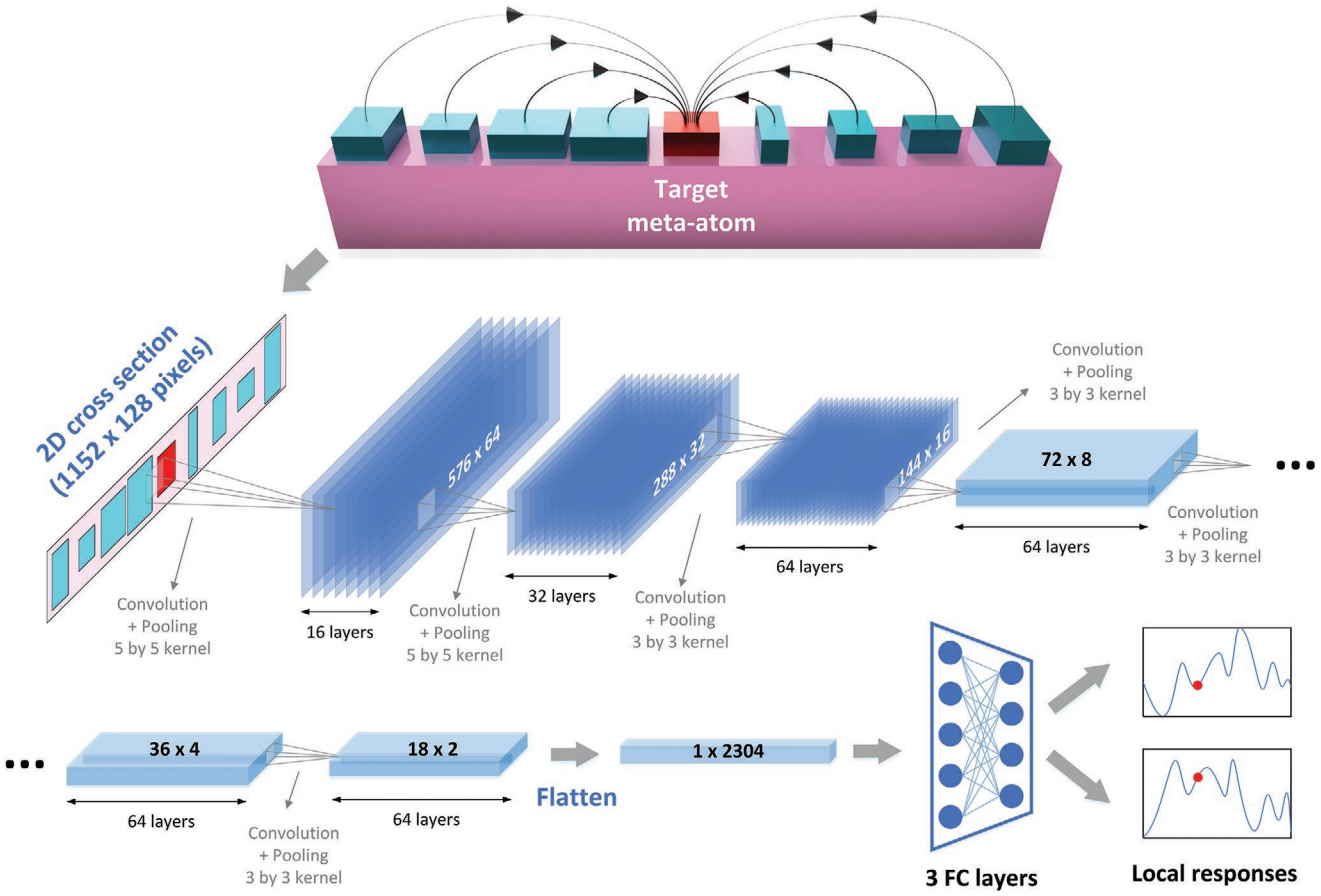

Figure 2. Network architecture. 2D cross-section containing the target meta-atom (in red) and its neighbors (in cyan) were processed through six consecutive convolution and pooling layers, then flattened into a 1D vector (1×2304). After being processed with three more fully connected layers (containing 512, 64, and 2 nodes, respectively), the real and imaginary parts of the transmission coefficients of the target meta-atom were retrieved.

predicted local responses are labeled with blue stars, while the accurate results calculated with CST are labeled with red starts. Excellent agreements have been achieved between the predicted and simulated results, while significant differences between the local responses and periodic-boundary responses can also be observed, which demonstrates the large impact of mutual coupling effects.

4. Results and Applications

With the help of this fully trained PNN, the local responses of the target meta-atoms (when deployed in a meta-device) can be predicted in milliseconds. This efficient and accurate tool enables optimization of metasurface devices that suffer from performance deterioration caused by mutual coupling. As shown in **Figure 4**a, we combined the PNN with a global optimization algorithm to inversely optimize the performance of metasurfaces. First, a conventional metasurface was designed based on the periodic boundary condition assumption and assigned as input. The PNN then evaluates the local responses of the current design. Subsequently, the optimization algorithm generates a new design, with dimensions of each element tuned to minimize the difference between the current responses and the design goal. The optimization process terminates when the stopping criteria are met or the maximum number of iterations is reached. A Dual Sequence Simulated Annealing Algorithm was adopted as the optimizer. We started with the optimization of a beam deflector and compared the performance of the optimized design with the initial design to demonstrate the efficacy of this optimization approach.

Figure 4b presents the optimization result of a beam deflector composed of periodic arrangements of 4 meta-atom unit cells. For the initial design shown in the left, periodic responses of each meta-atom are marked with squares in the polar plot, while their corresponding local responses (i.e., actual responses) are marked with open circles. The phase targets are set to 60°, 150°, 240°, and 330°, with the amplitude targets set to 1. Although the periodic responses are nearly perfect, with almost unity E-field amplitude and precise 90° phase shift between each pair of adjacent meta-atoms, their local responses deviate from the design goals due to the mutual coupling effects, resulting in low average efficiency (41.3%). We then started the optimization with this initial design and minimized the objective function, defined as

$$E = \frac{1}{N}\sum_{i=1}^{N}\sqrt{\left(\left(\nabla\Phi_i - \nabla\hat{\Phi}_i\right)/\pi\right)^2 + \left(A_i - \hat{A}_i\right)^2} \quad (2)$$

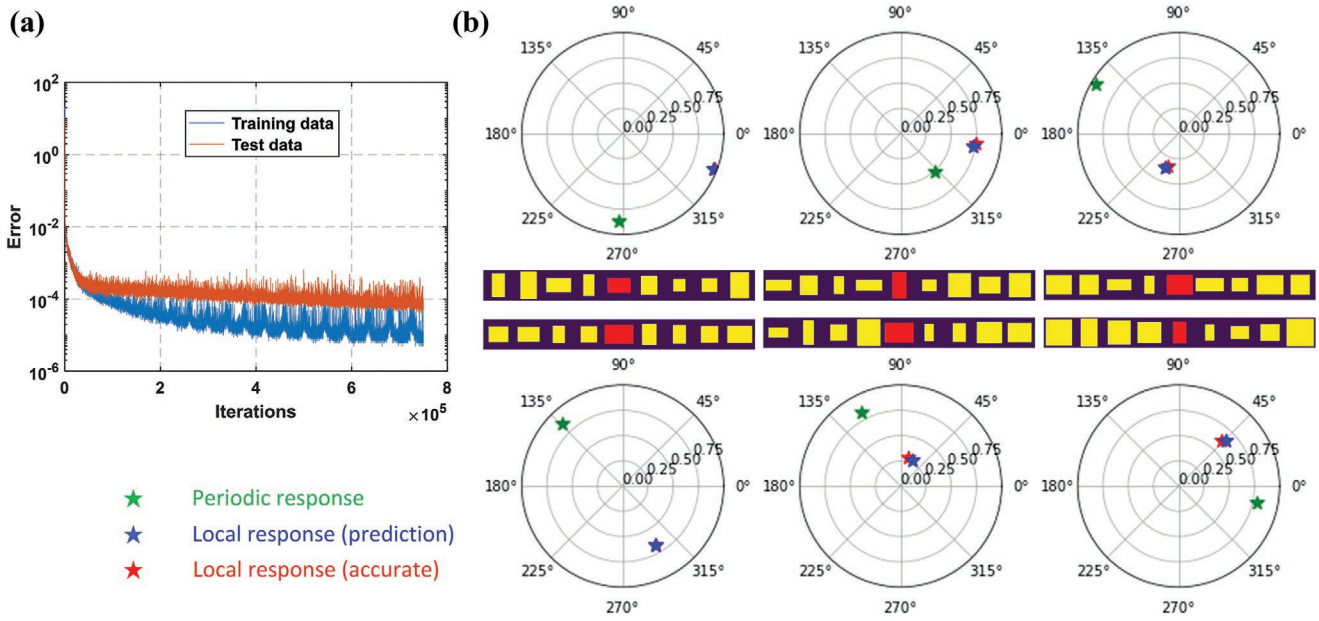

Figure 3. Learning curve and results. a) MSE of the training set (red curve) and test set (blue curve) during the training process. b) Phase-amplitude polar diagrams showing six groups of EM responses from randomly selected test set geometries. The target meta-atoms are marked in red, while the neighbors are marked in yellow. Periodic-boundary responses are labeled with green stars, while local responses predicted with PNN and calculated with CST are denoted with blue and red stars, respectively.

where N is the number of the meta-atoms in the device, Φ_i and A_i are the local phase and amplitude responses, $\hat{\Phi}_i$ and $\hat{A}_i$ are the target phase and amplitude responses, respectively. After 1000 iterations of optimization, the local responses of the optimized meta-atoms as shown on the right (Figure 4b) are much closer to the design goals, which also leads to a higher efficiency of 68.8%, meaning nearly 70% of the incident energy is deflected to the 1st order. Comparisons of the phase error and amplitude between the initial design and the optimized design are presented in Figure 4c. The values of the objective function during the optimization process are shown in Figure 4d, after which the average phase error has been reduced from 30.3° (initial design) to 10.4° (optimized design) while the average amplitude remains roughly the same, indicating the efficacy of the proposed approach.

The advantage of this combined optimization approach becomes even more evident when applied to larger size meta-devices, such as high numerical aperture (NA) metalenses. Here we designed a 1D cylindrical metalens composed of 40 meta-atoms (32 μm) with a focal length of 15.5 μm (NA = 0.72) using the conventional approach. The real part of the transmitted electric field of this lens as simulated with CST is shown in **Figure 5**a. Wavefront distortions produced by the initial metalens cause significant scattering of the transmitted energy, illustrated as nonconverging wavevectors in Figure 5a. The local phase responses of the meta-atoms in the initial design are shown in Figure 5b, where the phase error of each meta-atom is also calculated and plotted. Due to the symmetrical nature of the metalens, we only listed the responses of the meta-atoms in the right half. The phase errors between the targets and the local responses reach almost 100° for several meta-atoms. Subsequently, this initial design was set as a starting point for the optimization using the proposed network and the same objective function in Equation (2) was adopted. After 500 iterations of optimization (finished in 200 s), the local phase responses of the optimized meta-atoms (Figure 5c) are much closer to the targeted values, with the average phase error reduced from 30.4° to 10.4° (Figure 5d). Values of the objective function during the optimization are plotted in Figure 5e. As a result, the electric field magnitude at focal spot (z = 15.5 μm) increased from 3.24 to 4.17 V m^{-1}, equivalent to a 28.7% and 65.6% enhancement in electric field and intensity, respectively (Figure 5e). The focusing efficiency increases from 52.19% to 77.62% after the optimization. Here the focusing efficiency is defined as the ratio of the light that passes through an aperture with three times the FWHM focal spot size to the total electric field intensity that passes through the metalens. This clearly indicates that the transmitted energy is better focused due to the more accurate phase profile. To further demonstrate that this approach is compatible with full size metasurface designs, a high NA cylindrical metalens composed of 200 meta-atoms was also designed and optimized (Figure S3, Supporting Information).

5. Discussion and Conclusion

In this paper, we have quantified the effects of mutual coupling in metasurface designs and devised a novel way of quickly and accurately predicting the perturbed response of a specific meta-atom after being surrounded by different neighbors through a deep learning approach, which can be used to inversely optimize the design's performance. Although the presented PNN and optimizations are showcased on simple rectangular-shaped meta-atoms made of a common material (polysilicon) in the near infrared range (1550 nm), this approach can be extended

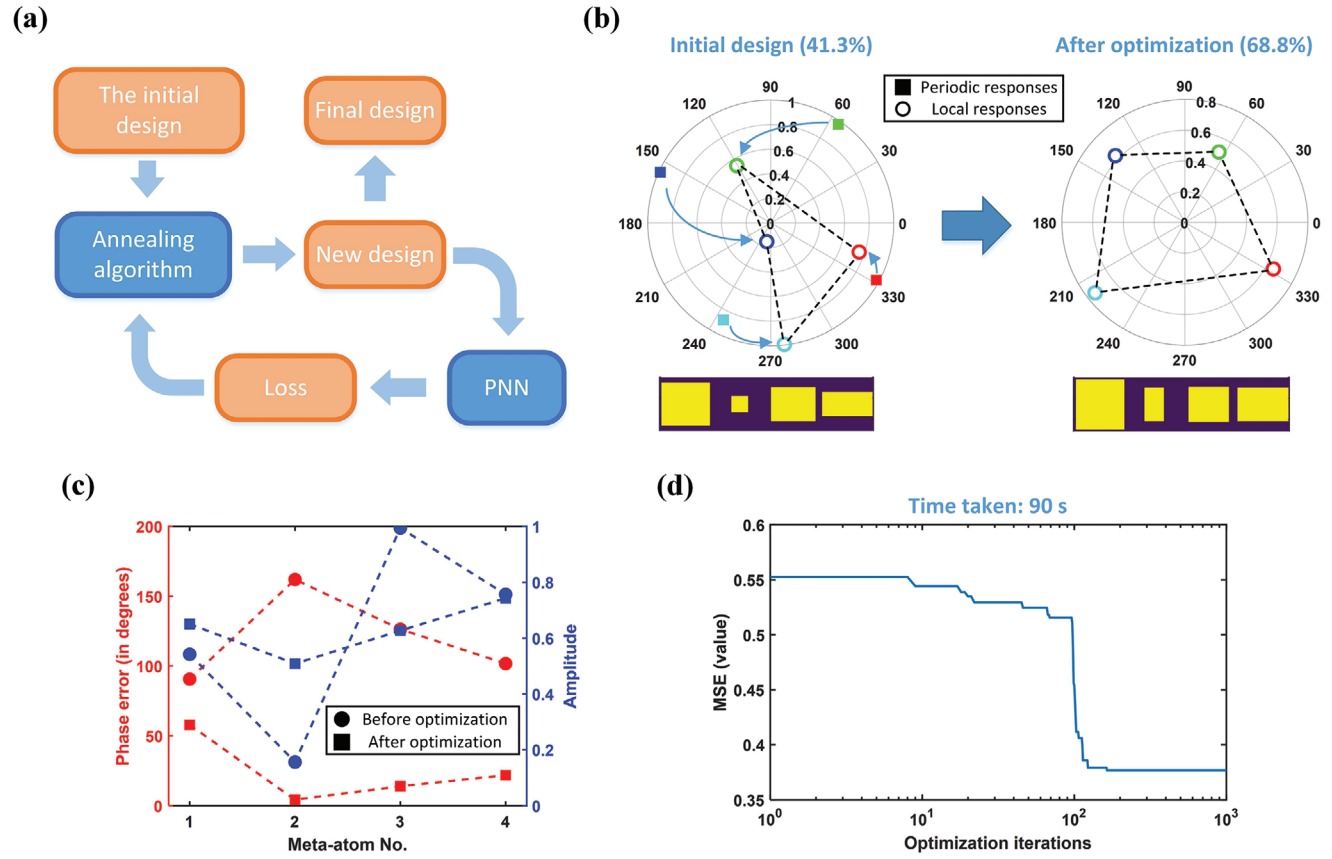

Figure 4. Optimization of a beam deflector composed of 1 × 4 meta-atoms. a) Flow chart of the combined optimization approach. b) Periodic responses and local responses of the initial design and the final optimized design. Top view of the two unit cells are shown on the bottom. Dielectric nanoblocks are yellow, while dark color represents the void. c) Phase error and amplitude of the optimized design compared to the initial design. d) Value of the objective function during the optimization.

to other materials, shapes, or working frequencies. Here we extend this mutual coupling analysis to another metasurface platform made by patterning a 1 μm thick film of high-index dielectric material ($n = 5$) placed on a low-index dielectric substrate ($n = 1.4$). The period is set to 2.8×2.8 μm^2, and the wavelength is 5.45 μm. In this case, to introduce more degrees of freedom, a 2D cross section of each meta-atom is defined by a complex image with resolution of 64 × 64 pixels. High index meta-atoms allow tighter field confinement and thus are less prone to mutual coupling (Figure S4, Supporting Information). Therefore, we only consider the influence of 2 neighbors on each side during the data collection process, which provides the same level of accuracy as the previous setup in Figure 1. Similarly, 100 000 groups of data were collected to assemble the training dataset, and the network architecture was slightly modified to accommodate the new input dimension (320 × 64). When the training was completed, the MSE was 2×10^{-5} for the training set and 6×10^{-5} for the test set, respectively (**Figure 6**a). Six meta-atoms were randomly selected from the test dataset to illustrate the network's accuracy (Figure 6b). Later in the Supporting Information, we verified that this approach can also be extended to 2D cases with similar accuracy.

Besides its applications in optimizing the performance of meta-devices, the proposed deep learning approach also provides an efficient way to explore the mutual coupling effects in existing designs. For example, utilizing this well-trained PNN, we are able to visualize the negative correlations between the metasurface's performance and the severity of the mutual coupling effects. For demonstration purpose, we generate numerous metasurface designs composed of individual meta-atoms with identical EM responses but different shapes. Specifically, we employed a Generated Adversarial Network (GAN) model to complete this task. Here, 400 meta-atoms were generated with a fully-trained GAN[31] that's capable of designing meta-atoms based on phase and amplitude targets. Among these 400 meta-atom designs, each group of 100 meta-atoms is created with the same amplitude target of 0.9 and different phase targets of 45°, 135°, 225°, and 315°, respectively (**Figure 7**a). Subsequently, one meta-atom was randomly selected from each set of 100 geometries to assemble a beam deflector consisting of 4 meta-atoms (the process flow is guided with red lines in Figure 7a,b). By repeating this process, a total number of 1000 beam deflectors were created and simulated with a full wave simulation tool to calculate their efficiencies and local responses. The relationship between the efficiency of each deflector and the MSE of all meta-atoms inside are plotted in Figure 7b. Although the periodic responses of these meta-atoms are almost identical, their corresponding local responses can be

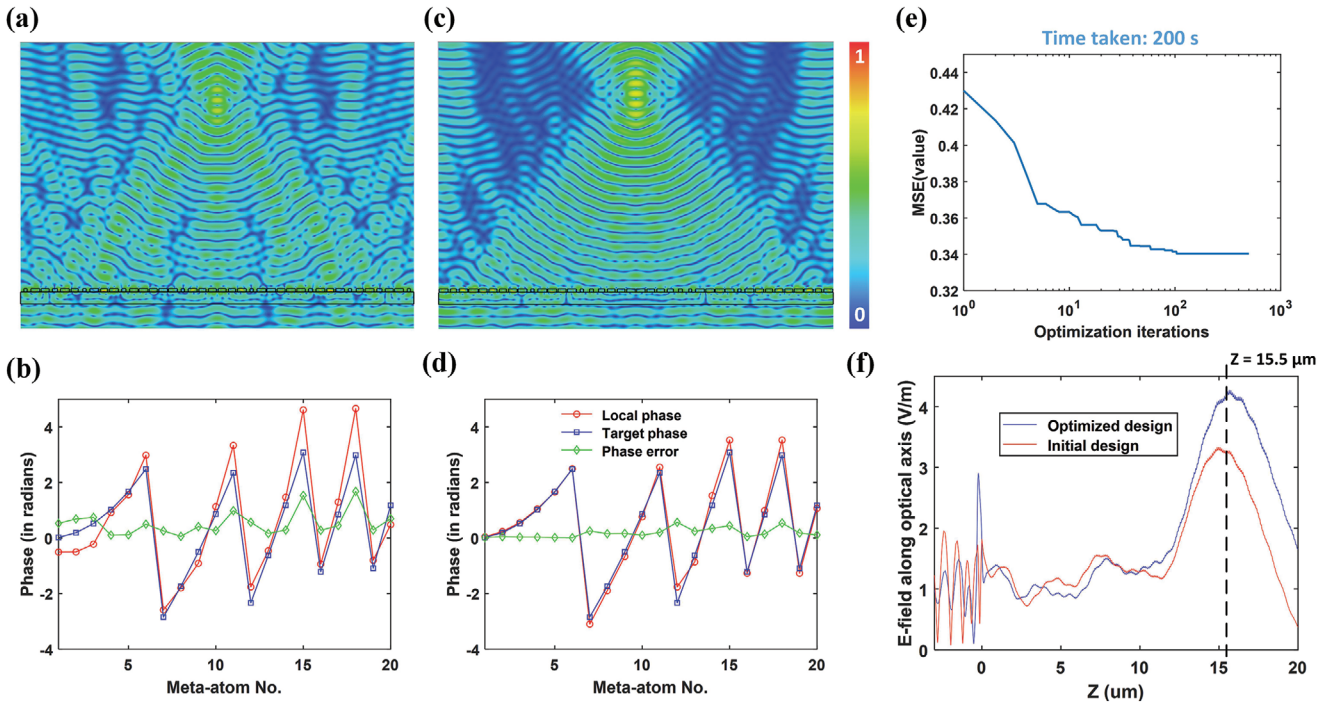

Figure 5. Optimization of a high numerical aperture metalens composed of 40 meta-atoms. a) Simulated electric field (real part) of the initial design, with target phase (blue), local phase (red), and phase error (green) of each meta-atom showing in b). c) Simulated electric field of the optimized design, with target phase, local phase, and phase error showing in d). e) Value of the objective function during the optimization. f) Simulated electric field magnitude along the optical (Z) axis, with an *x*-polarized incidence for the initial design (red) and the optimized design (blue).

very different when they are placed among different neighbors in a large array (Figure 7c) due to the mutual coupling effect. To better visualize the relationship between local responses and metasurfaces' performance, we plotted the electric field and local responses of two selected deflectors (Figure 7d) from these 1000 designs. The high efficiency (86.3%) designs shown on the right clearly have higher average amplitude and precise 90° phase shifts between adjacent meta-atoms as compared to their low efficiency (51.6%) counterparts shown on the left. The efficiency of each deflector among the 1000 designs ranges from

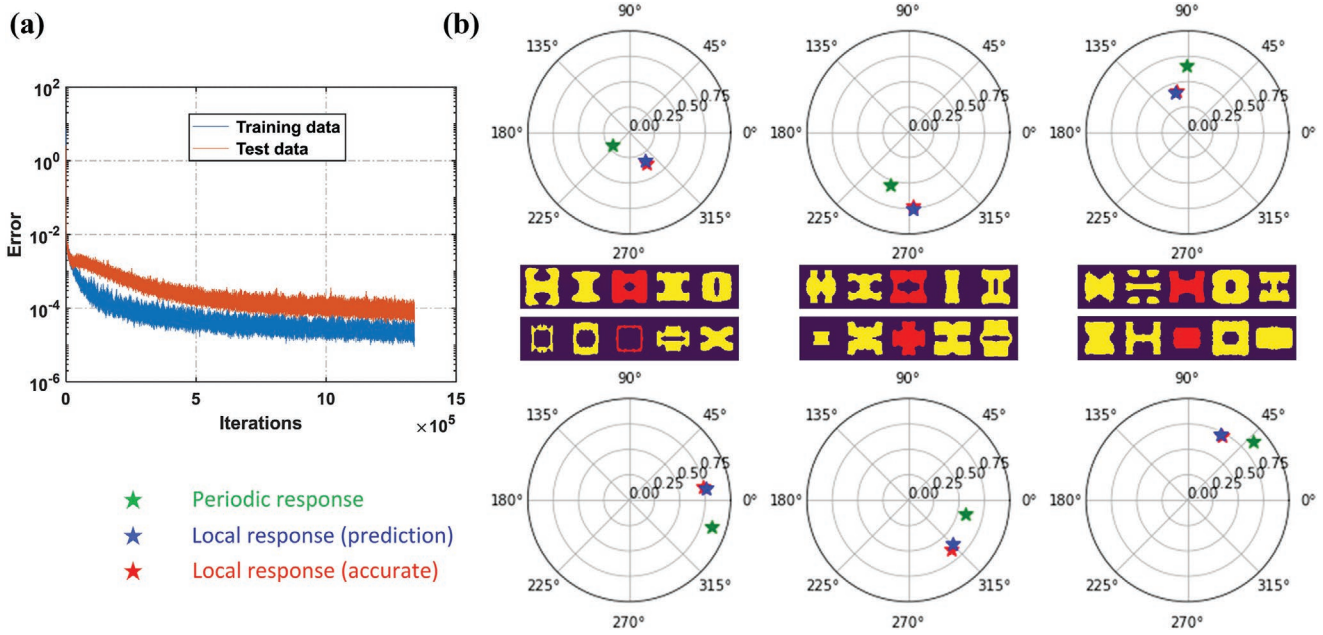

Figure 6. Learning curve and results. a) MSE of the training set (red curve) and test set (blue curve) during the training process. b) Six groups of results randomly selected from the test set are demonstrated.

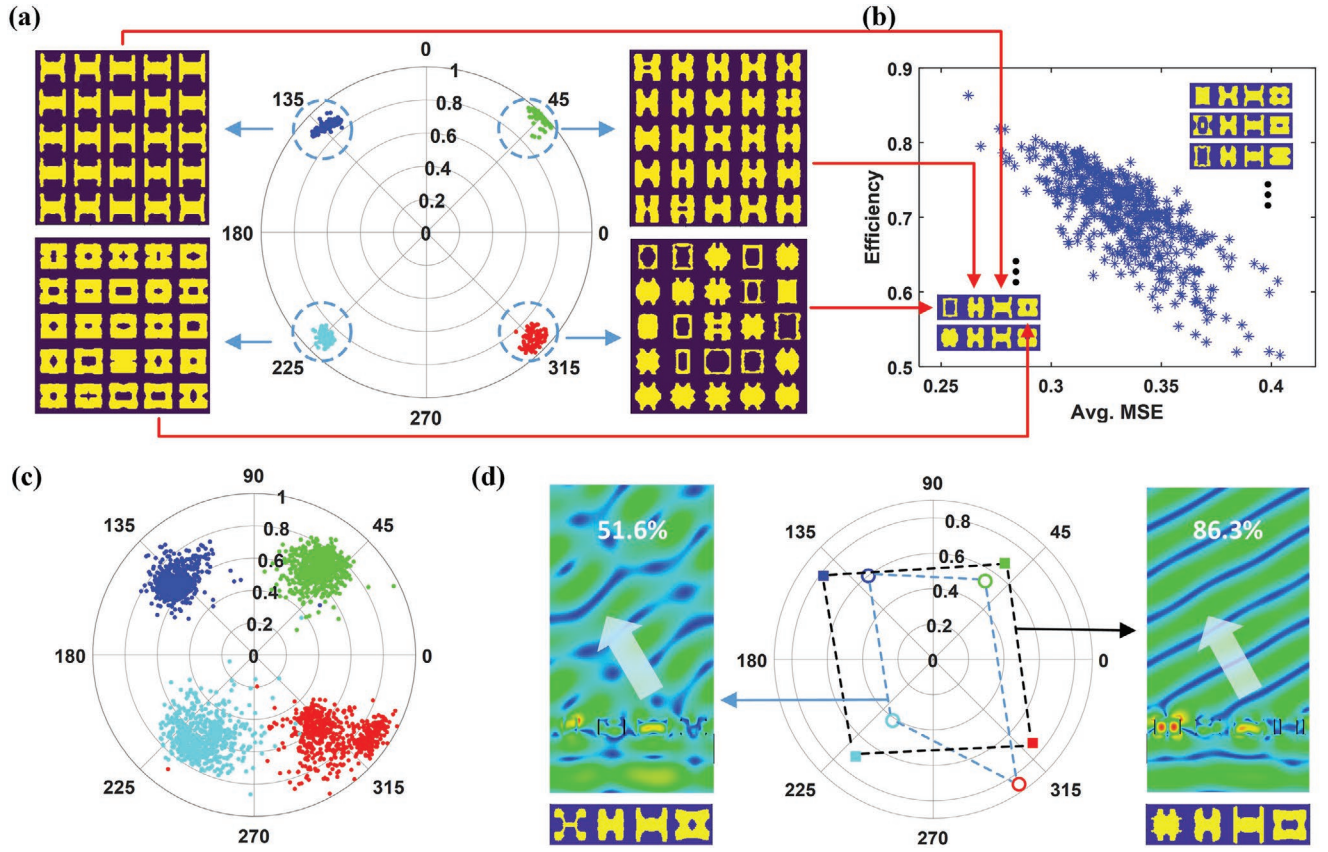

Figure 7. Extension to freeform meta-atoms built with high refractive index material. a) Periodic phase and amplitude responses of 400 meta-atoms generated with a fully-trained GAN model. Each group of 100 meta-atoms are created with the phase target: 45° (green), 135° (blue), 225° (cyan), and 315° (red), respectively. Several examples selected from each group are shown as insets. b) MSE versus efficiency of 1000 beam deflectors composed of 4 meta-atoms that were randomly selected with one from each group of meta-atoms in a). For demonstration, top views of several deflectors are included as insets. c) Corresponding local responses of all meta-atoms in the beam deflectors. d) Simulated electric field of two deflectors selected from b) and the local response of each meta-atom in these two designs.

only 50% to almost 90%, indicating that these high-index freeform mid-infrared metasurfaces also suffer from mutual coupling effects. Moreover, the obvious inverse correlation between the error and the overall efficiency demonstrates the feasibility of using the local responses to optimize the performance of a wide variety of metasurfaces.

A major advantage of this deep learning approach is time efficiency. Once fully-trained, the PNN calculates the local responses of target meta-atoms on a one-time calculation basis. As a result, when combined with different optimization algorithms, the PNN can evaluate the performance of the new designs instantly, without time-consuming fullwave simulation cycles. In conventional meta-optic optimization problems, the time-consuming fullwave validations have been the bottleneck of the whole design process. For example, one fullwave simulation of the metalens in Figure S3 (Supporting Information) takes over 30 min, which makes the iterative optimization of such a large structure nearly impossible. In contrast, the local responses and the objective function of the metalens can be calculated in seconds using the proposed approach, which can largely accelerate the adjoint optimization process. Moreover, parallel optimization algorithms and parallel computing can be introduced to further improve the computational efficiency.

The fabrication tolerance also plays a key role in determining the performance of fabricated meta-devices. It has been reported in previous literatures[40] that the efforts of increasing the efficiencies of meta-devices with optimization approaches could be diminished by manufacturing defects. In contrast, our proposed DNN approach has potentials to overcome this issue for two reasons: 1) The PNNs can predict the performance of meta-atoms in milliseconds, thus one can easily generate robust meta-atom designs that are resilient to fabrication defects using updated figure of merit with no additional time cost. 2) The PNNs trained with high-resolution input data can also deal with low-resolution inputs. For example, each meta-atom in the input images for PNN in Figure 2 are composed of 128×128 pixels, which assumes the minimum fabrication feature size is 6.25 nm. We can limit the resolution of generated designs to 64×64 (with the minimum feature size of 13 nm) or even coarse than that to make the generated designs compatible to the real fabrication capability. The PNNs can still handle the resized inputs with no further training needed.

A major challenge of this adjoint optimization approach is that the local responses of the meta-atoms cannot always meet the design goals. For example, the optimized beam deflector design in Figure 5b only achieved 68.8% efficiency, which is

still far from the theoretical limit. However, we believe that this issue can be addressed by introducing more degrees of freedom. For example, compared to the simple rectangular-shaped meta-atom design, the deflector assembled with freeform geometries in Figure 7d has the potential to achieve much higher efficiency (86%). Meanwhile, more-sophisticated global optimization approaches[22,46–48] such as evolution strategies[23,36,49,50] will be needed to deal with the massive design degrees of freedom brought by the freeform-shaped meta-atoms.

To conclude, we have proposed a deep learning network that accounts for mutual coupling effects to efficiently predict the local responses of target meta-atoms. The fully-trained network takes the dimension of a target meta-atom and its neighbors as input and generates its accurate local response in milliseconds. We have demonstrated the network's capability through the optimization of a beam deflector and a metalens with significantly improved performance. The proposed approach can also be extended to other metasurfaces with different materials, shapes, and working wavelength. Furthermore, we have unveiled and visualized the correlation between the devices' performance and local response errors using the well-trained network. We envision that this deep learning approach will lead to significant improvements in efficiency for large metasurface designs and to metasurface designs surpassing conventional optical components in many applications, including miniaturized optics, holography, and optical information processing.

Supporting Information

Supporting Information is available from the Wiley Online Library or from the author.

Acknowledgements

This work was funded under Defense Advanced Research Projects Agency Defense Sciences Office (DSO) Program: EXTREME Optics and Imaging (EXTREME) under Agreement No. HR00111720029.

Conflict of Interest

The authors declare no conflict of interest.

Data Availability Statement

The data that support the findings of this study, containing the local responses of rectangular-shaped meta-atoms (Figure 3) and freeform meta-atoms (Figure 6), are openly available at GitHub in the repository "Metasurface-mutual-coupling" of the "SensongAn" directory at https://github.com/SensongAn/Metasurface-mutual-coupling.

Keywords

deep learning, metasurfaces, mutual coupling, neural networks, photonics

Received: October 1, 2021
Published online: November 23, 2021

[1] P. Genevet, F. Capasso, F. Aieta, M. Khorasaninejad, R. Devlin, *Optica* **2017**, *4*, 139.
[2] A. Arbabi, Y. Horie, M. Bagheri, A. Faraon, *Nat. Nanotechnol.* **2015**, *10*, 937.
[3] M. Y. Shalaginov, S. An, F. Yang, P. Su, D. Lyzwa, A. M. Agarwal, H. Zhang, J. Hu, T. Gu, *Nano Lett.* **2020**, *20*, 7429.
[4] N. Yu, F. Capasso, *Nat. Mater.* **2014**, *13*, 139.
[5] X. Wang, J. Ding, B. Zheng, S. An, G. Zhai, H. Zhang, *Sci. Rep.* **2018**, *8*, 1876.
[6] Q. Wang, X. Zhang, Y. Xu, J. Gu, Y. Li, Z. Tian, R. Singh, S. Zhang, J. Han, W. Zhang, *Sci. Rep.* **2016**, *6*, 32867.
[7] A. Arbabi, E. Arbabi, S. M. Kamali, Y. Horie, S. Han, A. Faraon, *Nat. Commun.* **2016**, *7*, 13682.
[8] W. Zhao, H. Jiang, B. Liu, J. Song, Y. Jiang, C. Tang, J. Li, *Sci. Rep.* **2016**, *6*, 30613.
[9] M. I. Shalaev, J. Sun, A. Tsukernik, A. Pandey, K. Nikolskiy, N. M. Litchinitser, *Nano Lett.* **2015**, *15*, 6261.
[10] M. Khorasaninejad, Z. Shi, A. Y. Zhu, W.-T. Chen, V. Sanjeev, A. Zaidi, F. Capasso, *Nano Lett.* **2017**, *17*, 1819.
[11] L. Zhang, J. Ding, H. Zheng, S. An, H. Lin, B. Zheng, Q. Du, G. Yin, J. Michon, Y. Zhang, Z. Fang, M. Y. Shalaginov, L. Deng, T. Gu, H. Zhang, J. Hu, *Nat. Commun.* **2018**, *9*, 1481.
[12] M. Y. Shalaginov, S. An, Y. Zhang, F. Yang, P. Su, V. Liberman, J. B. Chou, C. M. Roberts, M. Kang, C. Rios, Q. Du, C. Fowler, A. Agarwal, K. Richardson, C. Rivero-Baleine, H. Zhang, J. Hu, T. Gu, *Nat. Commun.* **2021**, *12*, 1225.
[13] J. Ding, S. An, B. Zheng, H. Zhang, *Adv. Opt. Mater.* **2017**, *5*, 1700079.
[14] S. An, J. Ding, B. Zheng, Y. Lin, W. Zhang, H. Zhang "Quad-wavelength multi-focusing lenses with dual-wavelength meta-atoms", presented at CLEO: Science and Innovations, San Jose, CA, 14–19 May 2017.
[15] P. Lalanne, S. Astilean, P. Chavel, E. Cambril, H. Launois, *J. Opt. Soc. Am. A* **1999**, *16*, 1143.
[16] P. Lalanne, P. Chavel, *Laser Photonics Rev.* **2017**, *11*, 1600295.
[17] M. Decker, I. Staude, M. Falkner, J. Dominguez, D. N. Neshev, I. Brener, T. Pertsch, Y. S. Kivshar, *Adv. Opt. Mater.* **2015**, *3*, 813.
[18] C. Pérez-Arancibia, R. Pestourie, S. G. Johnson, *Opt. Express* **2018**, *26*, 30202.
[19] D. Colton, R. Kress, *Integral Equation Methods in Scattering Theory*, SIAM, Philadelphia, PA **2013**.
[20] J.-C. Nédélec, *Acoustic and Electromagnetic Equations: Integral Representations for Harmonic Problems*, Springer Science & Business Media, New York **2001**.
[21] C. Pfeiffer, A. Grbic, *Phys. Rev. Lett.* **2013**, *110*, 197401.
[22] S. D. Campbell, D. Sell, R. P. Jenkins, E. B. Whiting, J. A. Fan, D. H. Werner, *Opt. Mater. Express* **2019**, *9*, 1842.
[23] D. Sell, J. Yang, S. Doshay, J. A. Fan, *Adv. Opt. Mater.* **2017**, *5*, 1700645.
[24] R. Pestourie, C. Pérez-Arancibia, Z. Lin, W. Shin, F. Capasso, S. G. Johnson, *Opt. Express* **2018**, *26*, 33732.
[25] T. Phan, D. Sell, E. W. Wang, S. Doshay, K. Edee, J. Yang, J. A. Fan, *Light: Sci. Appl.* **2019**, *8*, 48.
[26] Z. Lin, S. G. Johnson, *Opt. Express* **2019**, *27*, 32445.
[27] D. Liu, Y. Tan, E. Khoram, Z. Yu, *ACS Photonics* **2018**, *5*, 1365.
[28] J. Jiang, D. Sell, S. Hoyer, J. Hickey, J. Yang, J. A. Fan, *ACS Nano* **2019**, *13*, 8872.
[29] Z. Liu, D. Zhu, S. P. Rodrigues, K.-T. Lee, W. Cai, *Nano Lett.* **2018**, *18*, 6570.
[30] W. Ma, F. Cheng, Y. Liu, *ACS Nano* **2018**, *12*, 6326.
[31] S. An, B. Zheng, H. Tang, M. Y. Shalaginov, L. Zhou, H. Li, M. Kang, K. A. Richardson, T. Gu, J. Hu, C. Fowler, H. Zhang, *Adv. Opt. Mater.* **2021**, *9*, 2001433.

[32] S. An, B. Zheng, M. Y. Shalaginov, H. Tang, H. Li, L. Zhou, J. Ding, A. M. Agarwal, C. Rivero-Baleine, M. Kang, K. A. Richardson, T. Gu, J. Hu, C. Fowler, H. Zhang, *Opt. Express* **2020**, *28*, 31932.
[33] S. An, C. Fowler, B. Zheng, M. Y. Shalaginov, H. Tang, H. Li, L. Zhou, J. Ding, A. M. Agarwal, C. Rivero-Baleine, K. A. Richardson, T. Gu, J. Hu, H. Zhang, *ACS Photonics* **2019**, *6*, 3196.
[34] Z. Liu, L. Raju, D. Zhu, W. Cai, *IEEE J. Emerg. Sel. Top. Circuits Syst.* **2020**, *10*, 126.
[35] J. Peurifoy, Y. Shen, L. Jing, Y. Yang, F. Cano-Renteria, B. G. DeLacy, J. D. Joannopoulos, M. Tegmark, M. Soljačić, *Sci. Adv.* **2018**, *4*, eaar4206.
[36] Z. Liu, D. Zhu, K. T. Lee, A. S. Kim, L. Raju, W. Cai, *Adv. Mater.* **2020**, *32*, 1904790.
[37] M. Y. Shalaginov, S. D. Campbell, S. An, Y. Zhang, C. Ríos, E. B. Whiting, Y. Wu, L. Kang, B. Zheng, C. Fowler, H. Zhang, D. H. Werner, J. Hu, T. Gu, *Nanophotonics* **2020**, *9*, 3505.
[38] B. Auguié, W. L. Barnes, *Phys. Rev. Lett.* **2008**, *101*, 143902.
[39] K. E. Chong, L. Wang, I. Staude, A. R. James, J. Dominguez, S. Liu, G. S. Subramania, M. Decker, D. N. Neshev, I. Brener, Y. S. Kivshar, *ACS Photonics* **2016**, *3*, 514.
[40] A. J. Ollanik, J. A. Smith, M. J. Belue, M. D. Escarra, *ACS Photonics* **2018**, *5*, 1351.
[41] H. Cai, S. Srinivasan, D. A. Czaplewski, A. B. Martinson, D. J. Gosztola, L. Stan, T. Loeffler, S. K. Sankaranarayanan, D. López, *npj Comput. Mater.* **2020**, *6*, 116.
[42] S. Tan, F. Yan, L. Singh, W. Cao, N. Xu, X. Hu, R. Singh, M. Wang, W. Zhang, *Opt. Express* **2015**, *23*, 29222.
[43] S. Lepeshov, Y. Kivshar, *ACS Photonics* **2018**, *5*, 2888.
[44] M. V. Zhelyeznyakov, S. Brunton, A. Majumdar, *ACS Photonics* **2021**, *8*, 481.
[45] L. Hsu, M. Dupré, A. Ndao, J. Yellowhair, B. Kanté, *Opt. Express* **2017**, *25*, 24974.
[46] Z. Lin, V. Liu, R. Pestourie, S. G. Johnson, *Optics Express* **2019**, *27*, 15765.
[47] R. J.-M. F. Pestourie, Assume Your Neighbor is Your Equal: Inverse Design in Nanophotonics, Dissertation, Harvard University, **2020**.
[48] R. Pestourie, Y. Mroueh, T. V. Nguyen, P. Das, S. G. Johnson, *npj Comput. Mater.* **2020**, *6*, 164.
[49] R. S. Hegde, in *Novel Optical Systems, Methods, and Applications XXII*, Proc. SPIE Vol. *11105*, SPIE, Bellingham, WA **2019**, p. 1110508.
[50] D. Sell, J. Yang, S. Doshay, R. Yang, J. A. Fan, *Nano Lett.* **2017**, *17*, 3752.